



# High area-capacity Mg batteries enabled by sulfur/copper integrated cathode design

Zhenfang Zhou<sup>a,1</sup>, Aobing Du<sup>b,1</sup>, Weijie Kong<sup>a</sup>, Zhuang Chen<sup>a</sup>, Zhonghua Zhang<sup>a,b,\*</sup>, Bingbing Chen<sup>c</sup>, Yitao He<sup>d</sup>, Shanmu Dong<sup>b</sup>, Zhenjiang Li<sup>a</sup>, Guicun Li<sup>a,\*</sup>, Guanglei Cui<sup>b,\*</sup>

<sup>a</sup> College of Materials Science and Engineering, Qingdao University of Science and Technology, Qingdao 266042, Shandong, China

<sup>b</sup> Qingdao Industrial Energy Storage Research Institute, Qingdao Institute of Bioenergy and Bioprocess Technology, Chinese Academy of Sciences, Qingdao 266101, Shandong, China

<sup>c</sup> Department of Energy Science and Engineering, Nanjing Tech University, Nanjing 211816, Jiangsu, China

<sup>d</sup> Department of Physics, Harbin Institute of Technology, Harbin 150001, Heilongjiang, China

## ARTICLE INFO

### Article history:

Received 31 December 2021

Revised 30 May 2022

Accepted 31 May 2022

Available online 9 June 2022

### Keywords:

Magnesium batteries

Sulfur cathode

Displacement reaction

Copper sulfides

## ABSTRACT

Rechargeable Mg batteries potentially display lower cost and competitive energy density compared with their Li-ion counterparts. However, the practical implementation of high area-capacity cathodes still remains a formidably challenging task. This work presents the sulfur/copper integrated cathodes fabricated by the conventional blade-coating process and slurry-dipping method. The sulfur/copper foil integrated cathodes deliver a high area-capacity of 2.6 mAh cm<sup>-2</sup> after 40 cycles, while the sulfur/copper-foam integrated cathode exhibits an ultrahigh area-capacity of 35.4 mAh cm<sup>-2</sup>, corresponding to 743.1 Wh L<sup>-1</sup> at the electrode level (1.5 times higher than the LiCoO<sub>2</sub>-graphite system). The in-situ formed copper sulfide intermediates with sufficient cation defects can act as functional intermediates to regulate the sulfur electrochemistry during the first discharge process. The subsequent cycles are operated by the reversible displacement reaction between Mg-ions and copper sulfide active substances. In particular, the copper ions prefer to extrude along the [001] direction in copper sulfides lattice and simultaneously the rock-salt MgS crystals are generated. Besides, the nonuniform surface topography of the cycled Mg-metal anode, caused by the spatial inhomogeneity in current distribution, is demonstrated to lead to the battery performance degradation for high area-capacity Mg batteries.

© 2022 Science Press and Dalian Institute of Chemical Physics, Chinese Academy of Sciences. Published by ELSEVIER B.V. and Science Press.

## 1. Introduction

The transition from fossil fuels to sustainable and clean energy applications, such as electric transportations and large-scale grid storage, calls for the development of battery technologies beyond Li-ion systems [1–3]. Rechargeable Mg batteries, normally comprised of a Mg-metal anode, undergo two-electron conversion electrochemistry. The utilization of Mg metal anode leads to staggering increases in volumetric capacity (theoretically 3833 Ah L<sup>-1</sup> for Mg anode vs. 2062 Ah L<sup>-1</sup> for Li metal anode and 841 Ah L<sup>-1</sup> for graphite anode) [4,5]. Rechargeable Mg-S batteries are expected to offer competitive energy density with lower cost and less safety concerns compared with the state-of-the-art Li-ion battery systems.

These unique advantages of Mg batteries drive a resurgence of research activities in this sector [6–9].

Despite these appealing merits, the development of Mg batteries is still in its infant stage [3,10]. The performance of the present cathode materials which exhibit low reversible capacity and fast capacity fade cannot meet the requirements of industry practicality. The low electron/Mg-ion transfer kinetics in cathode material lattice has been condemned as the main causation [11,12]. For low cost sulfur cathode, the extremely low free energy of the discharged products of MgS may be the essential determinant for sluggish sulfur conversion reaction since the complete decomposition of MgS requires quite high activation energy to break the strong electrostatic interactions. Recently, considerable efforts have been devoted to implementing reversible Mg batteries. Promising cathodes and efficient Mg-ion electrolytes have been developed [13–18]. However, sufficient improvement in reversible capacity and cycle life, especially under high area capacity conditions, still remains a great challenge.

\* Corresponding authors.

E-mail addresses: [zhangzh@qust.edu.cn](mailto:zhangzh@qust.edu.cn) (Z. Zhang), [guicunli@qust.edu.cn](mailto:guicunli@qust.edu.cn) (G. Li), [cuiql@qibebt.ac.cn](mailto:cuiql@qibebt.ac.cn) (G. Cui).

<sup>1</sup> These authors contributed equally to this work.

Recently, reversible conversion reactions based on the copper/silver insertion-into/extrusion-from chalcogenide hosts have been demonstrated to significantly boost the magnesiation kinetics, leading to high reversible capacity and fair rate performance [15,19–21]. In addition, the integration of copper current collector and electroactive sulfur/selenium cathode has been also revealed to deliver better charge-discharge properties compared to sulfur cathode utilizing aluminum/stainless steel substrates [22–28]. Nuli and co-workers firstly revealed the formation of copper sulfides for the sulfur/copper foil electrodes during cycling, which improved the compatibility between sulfur and electrolytes [25]. The formation of highly conductive copper dendrites and the cuprous ions solid/liquid equilibrium have been responsible for the boosted Mg-ion storage properties [24,27]. The unique lattice structures of the in-situ formed sulfides and selenides intermediates may also play key roles in driving the electrochemical charge-discharge processes. However, this vital aspect, from a perspective of molecular-level reaction pathway, is seldom understood. Besides, the sulfur/copper integrated cathode design that might enable cheap and high area-capacity secondary or primary Mg batteries, is rarely studied to our best knowledge.

Herein, we present a sulfur/copper integrated cathode (S@Cu electrode) design for superior Mg batteries. The rechargeable Mg batteries employing the S@Cu foil electrode deliver a high area-capacity of  $2.6 \text{ mAh cm}^{-2}$  even after 40 cycles. More embracingly, taking advantage of the large surface area and scaffolding struc-

ture, a primary Mg battery prototype based on the S@Cu foam cathode design exhibits an ultrahigh area-capacity of  $35.4 \text{ mAh cm}^{-2}$ , corresponding to  $743.1 \text{ Wh L}^{-1}$  at the electrode level. These achievements outperform the state-of-the-art results. Experimental and theoretical studies reveal that the chemical reaction between sulfur and copper in-situ forms copper sulfide intermediates, which facilitates the conversion from sulfur to MgS during the first discharge. The subsequent cycles are operated by highly reversible displacement reaction between Mg-ions and copper sulfide active substances. In particular, the copper ions are more likely extruded along the [001] direction of copper sulfide lattice and simultaneously the rock-salt MgS crystals are generated, during which the existence of copper ion defects is responsible for the phase transformation kinetics. Our work highlights the possibility to dramatically improve the sulfur utilization via a facile sulfur/copper integrated cathode design for high area-capacity Mg batteries.

## 2. Results and discussion

### 2.1. Design and performance of high area capacity Mg batteries

The sulfur/copper integrated cathodes were easily fabricated by the conventional blade-coating process (for the S@Cu foil electrode) and slurry-dipping method (for the S@Cu foam electrode) as schematically depicted in Fig. 1(a and b), respectively. The

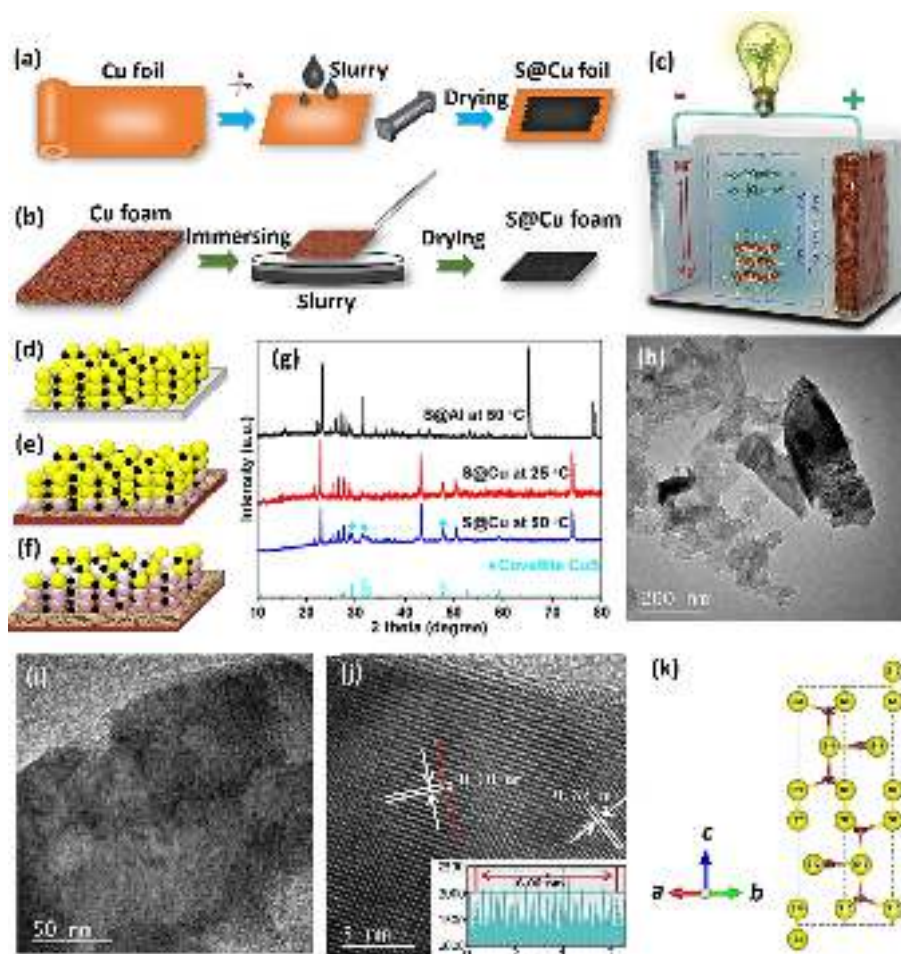


**Fig. 1.** Schematic illustration of the preparation processes for the S@Cu foil electrode (a) and the S@Cu foam electrode (b). Schematic illustration of Mg battery configuration using the S@Cu foam electrode and Mg-metal anode (c). Illustrations of varied cathodes (d: the S@Al foil electrode at 50 °C; e: the S@Cu foil electrode at 25 °C; f: the S@Cu foil electrode at 50 °C). XRD patterns (g) of varied cathodes. TEM (h and i) and HRTEM (j) images of the in-situ formed copper sulfide compound obtained from the S@Cu foil electrode. Inset in (j): the interplanar interspacing of the in-situ formed copper-sulfide compound. (k) The crystal structure of the in-situ formed copper sulfide compounds.

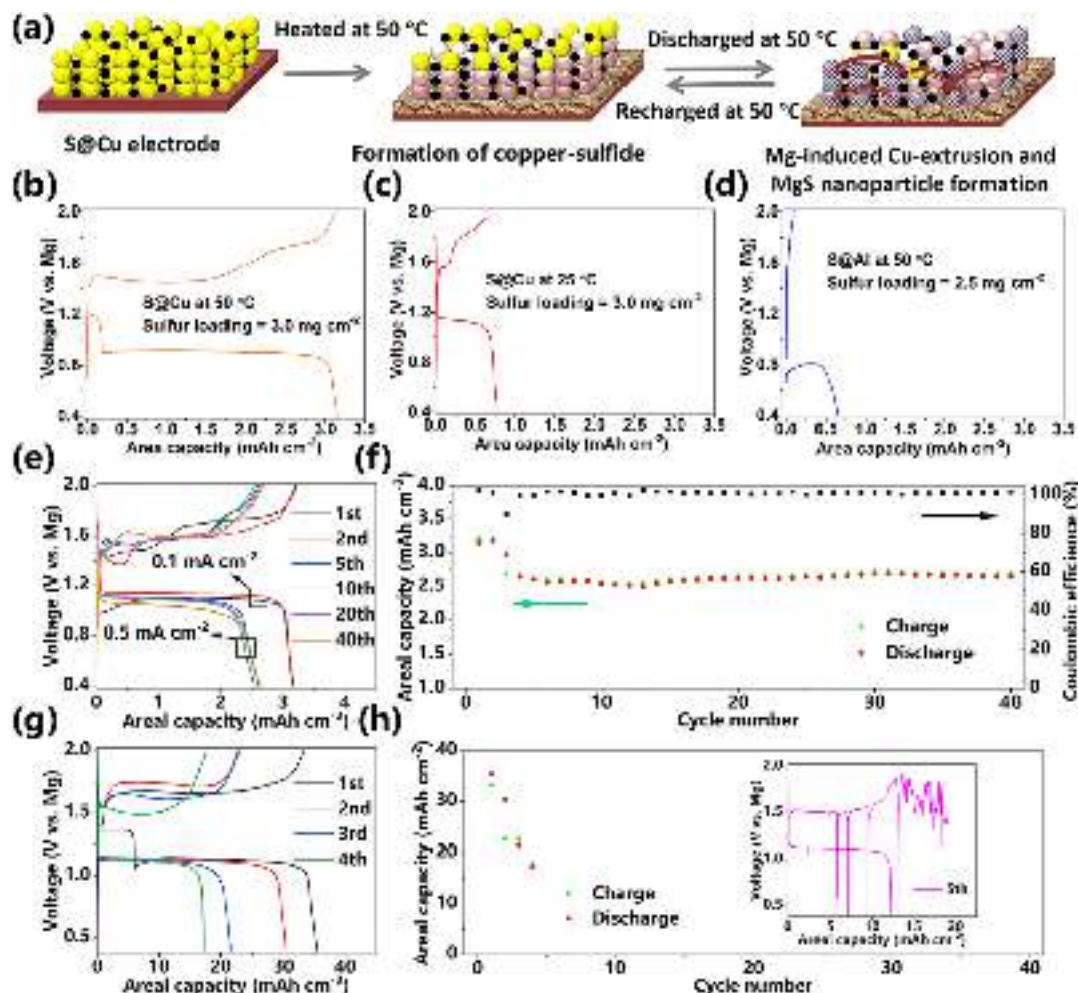


**Fig. 2.** (a) Schematic illustration of the in-situ formation of copper-sulfide intermediates and the reversible charge-discharge reaction mechanism. Galvanostatic charge-discharge profiles of the varied electrodes (b): the S@Cu foil electrode at 50 °C; c: the S@Cu foil electrode at 25 °C; d: the S@Al foil electrode at 50 °C). Galvanostatic charge-discharge profiles (e) and the cycle performance (f) of the S@Cu foil electrode. Galvanostatic charge-discharge profiles (g) and the cycle performance (h) of the S@Cu foam electrode. Inset in (h): the galvanostatic charge-discharge profile during the fifth cycle.

methods are rapidity, simplicity, and reliability in large-scale because no complicated instrument and expensive reagents are used. Secondary Mg batteries are constructed by the S@Cu foil electrode. The S@Cu foam electrode was employed as cathode for primary Mg batteries as ultrahigh sulfur mass loading may be accessible by virtue of the high surface area and the interconnected pore of copper foam scaffolds. Schematically shown in Fig. 1(c), the advanced Mg batteries are constructed by a Mg foil anode, a S@Cu integrated electrode, and the organic magnesium borate-based (OMBB) electrolytes. The operation of this cell is based on the conversion of sulfur to MgS assisted with the in-situ formed copper sulfide intermediates at the cathode and the Mg stripping/plating reaction at the anode side as discussed below.

For a conventional aluminum foil-supported sulfur electrode (abbreviated as “S@Al electrode”, shown in Fig. 1(d), there are no chemical or electrochemical reactions between sulfur and aluminum foil. This S@Al electrode displays poor discharge/charge reversibility even at 50 °C (Fig. 2d, shown below). This might be originated from the sluggish kinetics of pure sulfur electrode especially under a high sulfur mass loading condition of  $>2.0 \text{ mg cm}^{-2}$ . In sharp contrast, there is a severe chemical reaction between sulfur and copper foil as shown in Fig. 1(e), which can be accelerated at higher temperature of 50 °C (Fig. 1f), leading to the higher amount of copper sulfide compounds. This fact is revealed by X-

ray diffraction (XRD) patterns, transmission electron microscope (TEM), and high resolution transmission electron microscope (HRTEM) images. XRD peaks (Fig. 1g) are detected at  $29.3^\circ$  and  $31.8^\circ$ , corresponding to the (102) and (103) crystal plane of covellite CuS phase (PDF#: 06-0464). Typical TEM images in Fig. 1(h and i) reveal the sheet-like porous nanostructures of the copper sulfide compounds. Two representative lattice fringes with interlayer spacing of 0.30 and 0.32 nm (Fig. 1j) correspond to the (102) and (101) plane of covellite CuS phase, respectively. The crystal structure of covellite CuS phase is shown in Fig. 1(k), which exhibits a peculiar layered structure. Along the *c*-axis of this unusual crystal, triangular  $\text{Cu}_3\text{S}_3$  units and tetrahedral  $\text{Cu}_4\text{S}_4$  units are stitched together by more energetically favorable S–S covalent bonds.

The detailed microstructure of the S@Cu foam cathode (schematically shown in Fig. S1) presents a sandwich construction with copper as internal core and sulfur-copper sulfide composites as outer skin. Photographs in Fig. S2 illustrate the small-scale preparation and the weight ( $\sim 153.23 \text{ mg}$ ) of the S@Cu foam cathode. Typical scanning electron microscope (SEM) image (Fig. S3a) of pristine Cu foam displays a scaffolding structure with relative smooth surface. The irregular granular is observed on the surface of S@Cu foam cathode (Fig. S3b) indicating the in-situ formation of copper sulfide active substances. Sheet-like single crystal nature of copper sulfide active substances is confirmed by TEM image



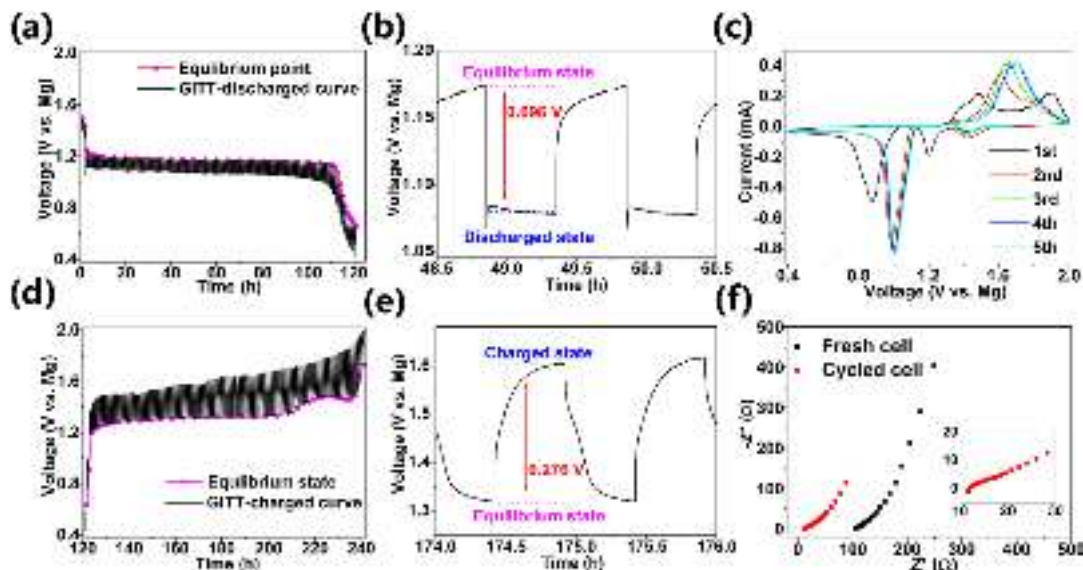


**Fig. 3.** GITT curve during the discharge process (a) and the detailed GITT curve (b) from 48.5 to 50.5 h. CV curves (c) of the S@Cu foil electrode. GITT curve during the recharge process (d) and the detailed GITT curve (e) from 174.0 to 176.0 h. EIS curves (f) of the fresh Mg-metal battery and cycled Mg-metal battery. Inset in (f): the close-up EIS curve from cycled cell.

(Fig. S3c). HRTEM image in Fig. S3(d) reveals the (101) and (103) plane of chalcocite  $\text{Cu}_2\text{S}$  with the interplanar spacing of 0.306 and 0.188 nm, respectively.

The formation of copper sulfide active substances and their electrochemistry are schematically illustrated in Fig. 2(a). Benefited from the in-situ formed copper sulfide active substances, the S@Cu foil electrode (Fig. 2b) displays a high area-capacity up to  $3.3 \text{ mAh cm}^{-2}$  at  $50^\circ\text{C}$ , which is almost 5 times higher than the S@Al electrode (only around  $0.7 \text{ mAh cm}^{-2}$ ) as shown in Fig. 2(d). It should be noted that at room temperature of  $25^\circ\text{C}$  the S@Cu foil electrode delivers rather poor reversible capacity as seen in Fig. 2(c). This might be ascribed to the low  $\text{Mg}^{2+}$  diffusion rate and the insufficient copper sulfide intermediates formation. To be specific, elevated temperature boosts the chemical reaction between sulfur and copper current collector (Fig. 2d–g), facilitating the formation of copper sulfide intermediates with better Mg-ion storage kinetics compared with that of sulfur cathodes. In addition, elevated temperature intrinsically improves the charge-discharge kinetics according to the classical Arrhenius equation, which indicates that the reaction rate constant increases exponentially with the temperature.

At a relative low current density of  $0.1 \text{ mA cm}^{-2}$ , the S@Cu foil electrode with sulfur mass loading of  $2.8 \text{ mg cm}^{-2}$  displays an initial specific capacity of  $1198 \text{ mAh g}^{-1}$  based on the mass of sulfur only (Fig. S4), corresponding to a high area-capacity of  $3.1 \text{ mAh cm}^{-2}$  (Fig. 2e). After switching the current density to  $0.5 \text{ mA cm}^{-2}$ , the S@Cu foil electrode displays a reversible specific capacity of  $900 \text{ mAh g}^{-1}$  and almost 100% Coulombic efficiency. A corresponding high reversible area-capacity of  $2.6 \text{ mAh cm}^{-2}$  is delivered even after 40 cycles (Fig. 2f). The S@Cu foil cathode with relatively low sulfur loading ( $2.2 \text{ mg cm}^{-2}$ ) displays a stable area-capacity of  $\sim 2.0 \text{ mAh cm}^{-2}$  from 10th to 80th cycle as shown in Fig. S5.

To achieve high area-capacity, the S@Cu foam electrodes have been utilized as cathodes. They show ultrahigh area-capacities ranging from  $12.9$  to  $34.2 \text{ mAh cm}^{-2}$  based on varied sulfur mass loading from  $12.5$  to  $33.3 \text{ mg cm}^{-2}$  (Fig. S6). Under an ultrahigh sulfur mass loading condition of  $\sim 30 \text{ mg cm}^{-2}$ , the S@Cu foam electrodes exhibit a reasonable discharge capacity of  $35.4 \text{ mAh cm}^{-2}$  during the first discharge process (Fig. 2g). This electrode can allow four charge/discharge cycles as shown in Fig. 2(h), which

has greatly restricted its application for secondary batteries. Future research works, such as interlayer design and anode modifications, might be helpful to improve its rechargeability, which is beyond the scope of this article. As shown in the cross-section SEM images in Fig. S7, the thicknesses of the S@Cu foil electrode and the S@Cu foam electrode are approximately  $132$  and  $524 \mu\text{m}$ , respectively. The volumetric energy densities of the S@Cu foil electrode and S@Cu foam electrode are calculated to be  $216.7$  and  $743.1 \text{ Wh L}^{-1}$ , respectively. These achievements are superior to previous reports as shown in Table S1.

To further examine the effect of current collector on sulfur electrochemistry, the electrochemical performance of the S@Ni foam electrode (fabrication is similar to that of the S@Cu electrode, but the reaction between sulfur and Ni foam is more sluggish than that between the sulfur and copper) is tested. As a result, the S@Ni foam electrode under a high sulfur mass loading condition of  $\sim 9.1 \text{ mg cm}^{-2}$  (Fig. S8) delivers so inferior capacity ( $2.1 \text{ mAh cm}^{-2}$  for initial discharge process and only  $0.01 \text{ mAh cm}^{-2}$  for the recharge process) and large overpotential. The as-constructed Mg batteries cannot operate for 2 cycles. These results undoubtedly demonstrate that the integration of sulfur electrochemistry with copper sulfide active substances contributes to the obtained high area-capacity.

## 2.2. Electrode kinetics of the copper sulfides-assisted sulfur cathodes

The electrochemical kinetics of the S@Cu foil electrode has been investigated by the galvanostatic intermittent titration technique (GITT), cyclic voltammetry (CV), and electrochemical impedance spectroscopy (EIS) experiments. The quasi-thermodynamic discharge voltage profile is tested using GITT as shown in Fig. 3(a), where the hollow red circles represent quasi-equilibrium voltage after fully relaxation. The thermodynamic value during discharge is approximately  $1.17 \text{ V vs. Mg}^{2+}/\text{Mg}$ . During the discharge process, the voltage hysteresis of the S@Cu foil electrode is only  $0.096 \text{ V}$  (Fig. 3b), while the charge voltage hysteresis is about  $0.276 \text{ V}$  (Fig. 3d and e). This indicates the much more sluggish oxidative conversion for the final discharged products of MgS. The total charge/discharge voltage difference is around  $0.53 \text{ V}$ , which is substantially lower value comparing to most of cathode materials for Mg batteries [11,29,30].

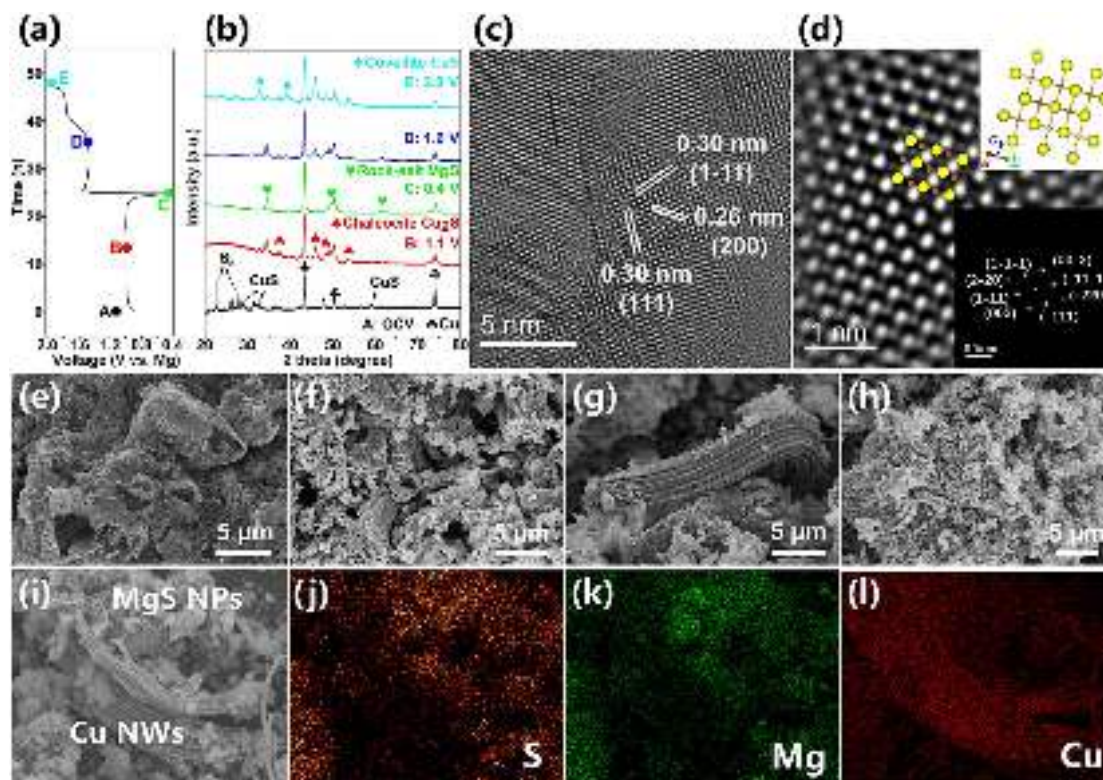


**Fig. 4.** Galvanostatic charge-discharge profiles (a) and the corresponding XRD patterns (b) of the S@Cu foil electrode at different charge-discharge states. The atomic-resolution aberration-corrected TEM image (c) and IFFT image (d) of the finally discharged products. Insets in (d): the crystal structure of MgS and the FFT pattern of selected area. SEM images of the S@Cu foil electrode at varied charge-discharge states (e: OCV; f: discharged to 1.1 V; g: at the end of discharge; h: recharged to 1.6 V). EDS mapping images (i–l) of the final discharged products.

Fig. 3(c) displays the CV curves of the S@Cu foil electrode at a scan rate of  $0.01 \text{ mV s}^{-1}$ . Two cathodic peaks at 1.20–1.24 and 0.86–0.89 V may correspond to the reduction of  $\text{S}_8$  to soluble polysulfides/copper sulfides and the subsequent reduction of polysulfides/copper sulfides to MgS, respectively. It should be noted that copper sulfide active substances might involve the reaction process, leading to a unique reaction pathway and thus a distinctive high current response for CV peak at lower voltage. The two anodic peaks located at 1.40–1.50 and 1.85–1.90 V may be associated with the oxidation of MgS to polysulfides and their subsequent transformation to copper sulfide species. The cathodic peaks shift to higher reduction potentials of 1.40 and 1.00 V after initial cycle, indicating improved conversion reaction and kinetics of the phase transformation from sulfur/copper sulfides to MgS after cell cycling. The anodic peaks progressively evolve to one broad peak at 1.65–1.80 V during the following cycles. After the initial scan, all CV profiles show stable charge/discharge peak positions, demonstrating the excellent electrode reversibility.

The cell impedance is monitored under OCV (open circuit voltage) condition as shown in Fig. 3(f). The large cell resistance of the fresh cell may be ascribed to the insufficient wettability of both cathode and anode with electrolytes. After the electrochemical activation process, the cell resistance drops to an acceptable value of  $11.8 \Omega$ . These above kinetic analyses illustrate the small electrode overpotential, high reversibility, and low internal resistance for the Mg batteries using the sulfur/copper integrated cathode.

### 2.3. Investigation of cathode reaction mechanism

To unveil the underlying charge-storage mechanism of the S@Cu foil electrode, the ex-situ experiments have been conducted. The ex-situ XRD experiments are conducted to monitor its phase

evolution in Fig. 4(a and b). A mixture of orthorhombic sulfur (PDF#: 08-0247) and trace of hexagonal copper sulfides (in the form of covellite  $\text{CuS}$  phase, PDF#: 06-0464) is detected from the XRD pattern in the fresh S@Cu foil electrode at OCV. After discharging to 1.1 V (point B), the XRD peak of sulfur completely disappears and rock-salt MgS crystal phase (PDF#: 35-0730) together with a new phase of hexagonal  $\text{Cu}_2\text{S}$  (chalcocite, PDF#: 26-1116) are detected. At the final discharged state of point C (Fig. 4b and Fig. S9), the XRD patterns of the discharged products dominantly show a binary mixture of rock-salt MgS and metallic copper.

The complete conversion from sulfur to MgS is crucial to attain high active material utilization and high specific capacity. Contrary to Dominko' reports that the electrochemically precipitated MgS cannot be detected by XRD technique, our results definitely confirm the formation of well-crystallized MgS phase with rock-salt structure [6,31]. This discrepancy might stem from the insufficient amount of MgS due to the low sulfur mass loading (merely  $0.75 \text{ mg cm}^{-2}$ ) in previously reported Mg-S cells [6,31]. The atomic-resolution aberration-corrected TEM image (Fig. 4c) of the finally discharged products of MgS clearly confirms the lattice fringes of MgS (111) and (200) with  $d$ -spacings of 0.30 and 0.26 nm, respectively. From the inverse fast Fourier transform (IFFT) image (Fig. 4d), it shows an (abcabc) sulfur stacking sequence parallel to (111) plane of MgS crystal in consistent with its crystal structure as shown in the inset of Fig. 4(d). The fast Fourier transform (FFT) (inset image in Fig. 4d) pattern with a zone axis of  $[110]$  reveals one set of diffraction spots that correspond to the rock-salt MgS crystals. Directly visualizing the arrangement of lattice sulfur and magnesium atoms firstly provides a strong evidence for the electrochemical formation of rock-salt MgS crystals.

The characterized XRD peaks at point D of chalcocite  $\text{Cu}_2\text{S}$  active substances re-appear. At the fully recharged states (point E), XRD



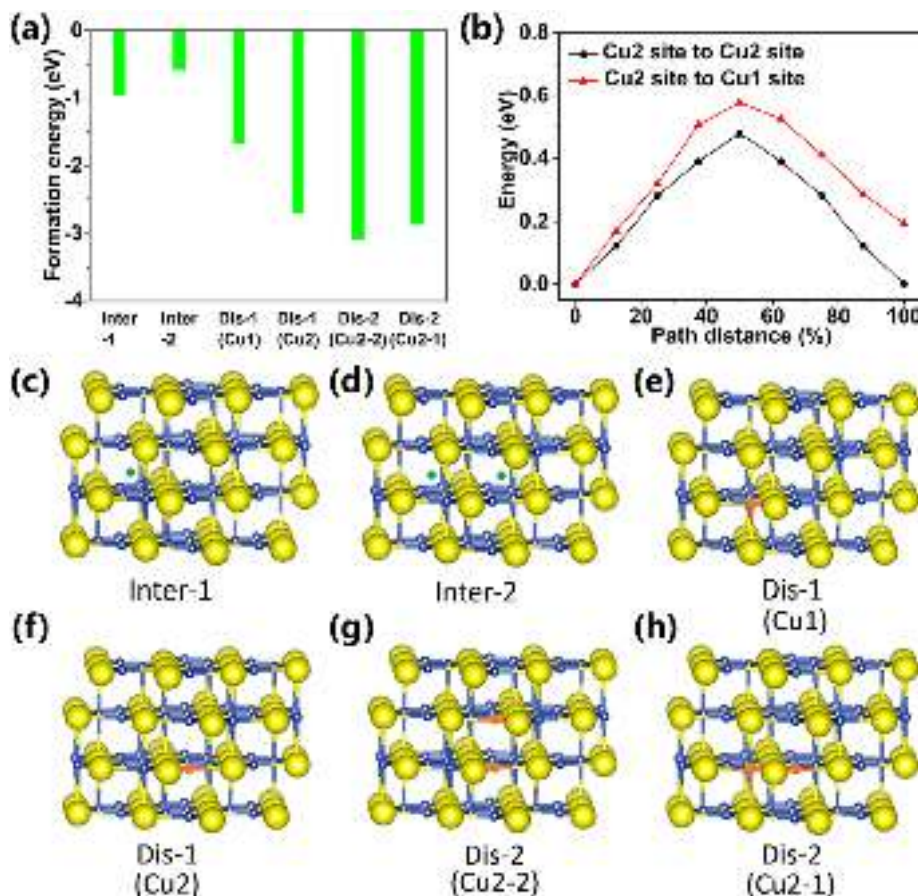


**Fig. 5.** The formation energy (a) of the copper sulfide with varied magnesian states. The activation barriers (b) for different diffusion pathways of Mg ions in defect-rich copper sulfide. The corresponding magnesian states: (c) intercalating one  $\text{Mg}^{2+}$ ; (d) intercalating two  $\text{Mg}^{2+}$ ; (e) displacing one  $\text{Mg}^{2+}$  at Cu1 site; (f) displacing one  $\text{Mg}^{2+}$  at Cu2 site; (g) displacing two  $\text{Mg}^{2+}$  at Cu2-Cu2 site; (h) displacing two  $\text{Mg}^{2+}$  at Cu2-Cu1 site.

peaks of MgS phase disappear and there are only the crystal phases of several copper sulfides including chalcocite  $\text{Cu}_2\text{S}$  and chalcocite-Q  $\text{Cu}_{1.96}\text{S}$ , which is consistent with TEM analysis (Fig. S10). Worth noting is that no sulfur crystal phases are detected by XRD technique. This indicates that the subsequent charge-discharge cycles might be based on the reversible conversion of these in-situ formed copper sulfide active substances. The ex-situ SEM images also reveal the dramatic morphology changes of the S@Cu foil electrode during cycling as shown in Fig. 4(e–h) and Fig. S11. Elemental mapping (Fig. 4i–l) investigations explicitly reveal that the long-range wire structures are dominant copper while the large particles around wires are mainly composed of S and Mg elements.

From the X-ray photoelectron spectroscopy (XPS) curve (Fig. S12) of the pristine S@Cu foil electrode, F, O, C, S elements are mainly detected. The pristine S@Cu foil electrode shows one dominant couple of S  $2p_{3/2}$  and S  $2p_{1/2}$  characteristic peaks at 164.2 and 165.4 eV, indicating the presence of sulfur element ( $\text{S}^0$ ) (Fig. S12b) [32,33]. When the electrode is discharged to 1.1 V, the S  $2p_{3/2}$  and S  $2p_{1/2}$  characteristic peaks are split into two couple peaks located at 161.9/163.0 and 163.8/165.1 eV, which are ascribed to the MgS and the  $-\text{S}-\text{S}-$  species in copper sulfides [33,34]. With further discharging to 0.4 V, the peak positions show minor changes while the atomic ratio between the MgS and the  $-\text{S}-\text{S}-$  species increases from 46/54 to 64/36, indicating the gradual transformation of copper sulfides to MgS during discharging (Fig. S12c). During the recharge processes, the S  $2p_{3/2}$  and S  $2p_{1/2}$  characteristic peaks positions show negligible changes while the relative peak area of the MgS and the  $-\text{S}-\text{S}-$  species displays dramatic decrease to 32/68, indicating the reversible conversion

reaction based on the in-situ formed copper sulfide active substances.

The formation of highly conductive copper nanowires and ultra-fine MgS nanoparticles facilitates the fast electron/ion diffusion, which should be responsible for the performance improvement of the high sulfur mass loading sulfur/copper integrated cathodes. In another aspect, the unique reaction pathway of S to MgS with the assistance of copper sulfide intermediates might also play a vital role in boosting the conversion kinetics of the high mass loading sulfur cathodes. The rechargeability of the final products (MgS and copper) has also been demonstrated by the MgS@Cu electrode in Fig. S13. Our results illustrate the critical role of copper in realizing the Mg-ion storage reversibility for sulfur cathodes.

In general, during the discharging process of the S@Cu foil cathodes, it is easy to conclude that copper sulfide (covellite  $\text{CuS}$  and chalcocite  $\text{Cu}_2\text{S}$ ) compounds, chemically or electrochemically generated and decomposed, inevitably change the conversion mechanism of sulfur electrode. This typically undergoes the gradual solid-liquid-solid phase transitions among sulfur, polysulfides, copper sulfides, and final MgS. The possible conversion of S into MgS with the assistance of copper sulfide compounds may occur in a unique reaction pathway: (1) the sulfur is reduced into the liquid-like polysulfide cathodes; (2) copper sulfides are chemically and/or electrochemically generated when copper foil comes into contact with sublimed sulfur and/or polysulfides cathodes; (3) a displacement reaction may occur in these copper sulfides and completely generate the final discharged products of highly porous rock-salt MgS nanoparticles and micro-sized metallic copper wires.

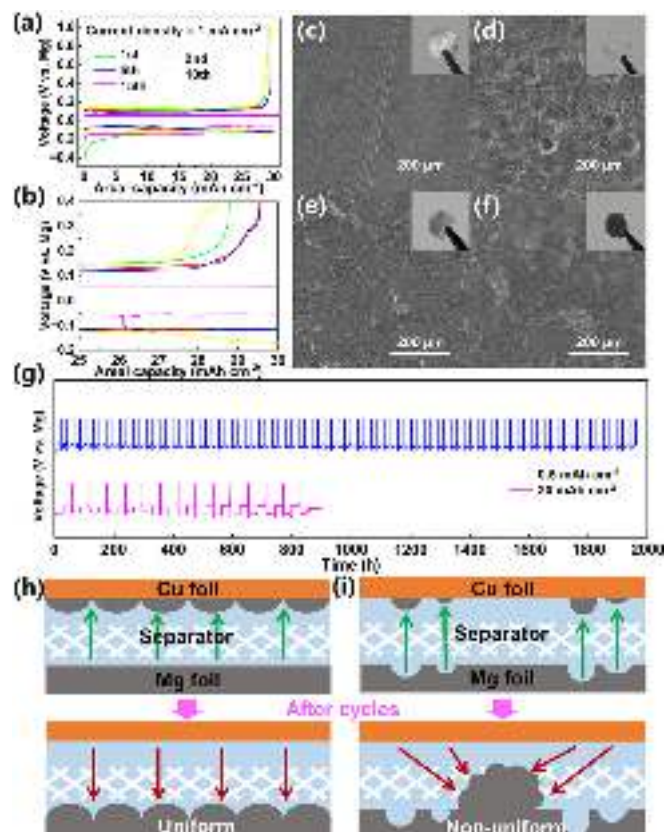


**Fig. 6.** The voltage-capacity profile (a) of the Mg stripping/plating processes with a practical cycling capacity of  $30 \text{ mAh cm}^{-2}$ . (b) Displays the magnified profile at a capacity range from  $25$  to  $30 \text{ mAh cm}^{-2}$ . SEM images of the pristine Mg anode (c), the initially stripped Mg anode (d), the first deposited Mg anode (e), and the deposited Mg anode after 15 cycles (f). Insets in (c–f): the corresponding digital photographs of Mg anodes. Comparison (g) of the cycling performance of Mg stripping/plating processes with a practical cycling capacity of  $0.5$  and  $30 \text{ mAh cm}^{-2}$ . Schematic illustration of the desired (h) and practical (i) Mg stripping/plating processes.

#### 2.4. Thermodynamic propensity of the cation displacement reaction

In order to clarify the specific effect of copper sulfide on the reaction mechanism, we focus on the thermodynamic characteristics of the replacement reaction between magnesium ion and copper sulfide. The intrinsically unstable nature of copper sulfides, which exhibits fairly complicated atomic arrangements and stoichiometries, makes it beneficial for the formation of a series of copper-deficient  $\text{Cu}_{2-x}\text{S}$  phases [35]. The thermodynamic propensity to form Cu deficiency equips the randomly distributed  $\text{Cu}^+$  with extremely high mobility (some are superionic with liquid-like mobility), which plays a pivotal role in activating the electrochemical reaction between  $\text{Mg}^{2+}$  and  $\text{Cu}_{2-x}\text{S}$  [36].

In order to demonstrate the presence of Cu defects, XPS spectra of the S@Cu foil electrode after soaking in OMBB electrolytes have been investigated as shown in Fig. S14(a). It is worth noting that after electrolytes soaking for 12 h, the chemical conversion reaction between sulfur and copper and the chemical replacement reaction between  $\text{Mg}^{2+}$  in electrolytes and  $\text{Cu}^+$  in the in-situ formed  $\text{Cu}_2\text{S}$  compounds spontaneously occur. This generates a great deal of cation-deficient  $\text{Cu}_2\text{S}$  (at peaks of  $163.6/162.4 \text{ eV}$ ) in the surface of the electrode, which has been demonstrated by the S 2p XPS spectra as shown in Fig. S14(a). Besides, the presence of  $\text{Cu}_2\text{S}$  signal indicates that the copper valence is approximately +1. It is generally known that the feature of UV-vis spectra is sensitive to the atomic ratio of Cu and S in the copper sulfide compounds. As

shown in Fig. S14(b), the UV-vis spectra of solid-state  $\text{Cu}_2\text{S}$  show a characteristic absorption band in near-infrared region, whereas the much weaker absorption band is detected for the  $\text{Cu}_2\text{S}$  after ball-milling. This result indicates that the irregular arrangement of surface atoms is responsible for the absorption band shift. As for the S@Cu foam electrode after soaking in OMBB electrolytes for 12 h, it shows much weaker characteristic absorption band in near-IR region, indicating the more amount of the Cu-defects in the in-situ formed copper sulfide compounds. The S@Cu foil electrode after cycling also displays weaker absorption band in near-IR region, indicating the presence of cuprous defects. In addition, the corresponding PL (photoluminescence) spectra (Fig. S14c) display a slightly red-shift for the electrolytes-soaked S@Cu foam electrode. And there is an additional emission peak at around of  $700 \text{ nm}$ , which relates to the defect state of the copper compounds. These above analyses provide strong evidences for the Cu defects in the in-situ formed copper sulfide compounds.

By using density functional theory (DFT) calculations, the formation of  $\text{MgS}$  from the defect-rich  $\text{Cu}_{2-x}\text{S}$  is demonstrated to be energetically favorable via a displacement reaction. As shown in Fig. 5(a–c), intercalating one  $\text{Mg}^{2+}$  into the tetrahedral interstitial sites results in a formation energy at  $-0.96 \text{ eV}$ , which increases to  $-0.58 \text{ eV}$  if two  $\text{Mg}^{2+}$  are intercalated into  $\text{Cu}_2\text{S}$ . In consideration of the existence of Cu vacancies (in  $\text{CuS}_4$  tetrahedron coordination (Cu1 site) and in  $\text{CuS}_3$  triangular coordination (Cu2 site)), the formation energies are calculated to be extremely low ( $-1.67$  and  $-2.70 \text{ eV}$ , respectively). Analysis of the formation energy confirms that the remarkably lower formation energy can be accommodated via a displacement reaction between defect-rich copper sulfides and  $\text{Mg}^{2+}$  compared to the intercalation of  $\text{Mg}^{2+}$  into the stoichiometric copper sulfides. This also indicates that the existence of Cu vacancies plays key roles in driving and governing the displacement reaction in these copper sulfide polymorphs.

In order to identify the  $\text{Mg}^{2+}$  diffusion pathway, the formation energy by adding another  $\text{Mg}^{2+}$  in  $\text{Cu}_2\text{S}$  at varied coordination conditions is calculated as shown in Fig. 5(d–h). Displacing additional Cu1 site with  $\text{Mg}^{2+}$  further decreases the formation energy to  $-2.9 \text{ eV}$ . Copper ion vacancy in  $\text{CuS}_3$  triangular coordination site (Fig. 5g) is more easily displaced by  $\text{Mg}^{2+}$  as indicated by the lower formation energy of  $-3.1 \text{ eV}$ . To gain insight into the migration behavior of Mg-ions in  $\text{Cu}_2\text{S}$  with the existence of Cu defects, the activation barriers of two predicted diffusion pathways (see Fig. S15 and Fig. 5b) are examined by nudged elastic band calculations. Between two low-energy Cu-defect sites of (Cu2 to Cu2), a maximal activation energy barrier of  $0.48 \text{ eV}$  is required for the hopping of Mg ions, while it is  $0.58 \text{ eV}$  for Mg ions migration from Cu2 site to Cu1 site. Considering that the ion diffusion rate is exponentially dependent on the activation energy, the “Cu2 to Cu2” diffusion rate may be one order of magnitude higher than that of “Cu2 to Cu1” pathway.

These results indicate the detailed displacement reaction between  $\text{Cu}_2\text{S}$  and  $\text{Mg}^{2+}$ , in which copper ions are more likely extruded along the [001] direction. Considering the intrinsically unstable nature and the low formation energy of defects, the displacement reaction may be thermodynamically favorable in these copper sulfide active substances. The small migration barrier of  $\text{Mg}^{2+}$  in  $\text{Cu}_2\text{S}$  with Cu vacancies also indicates that these copper sulfides may be viable cathode candidates for Mg batteries and should yield reasonable capacity even for a micrometer-sized particle.

#### 2.5. Degradation mechanism of primary Mg batteries with S@Cu foam electrode

As discussed above, although high area-capacity could be implemented by the S@Cu foam electrodes, they suffer from rapid



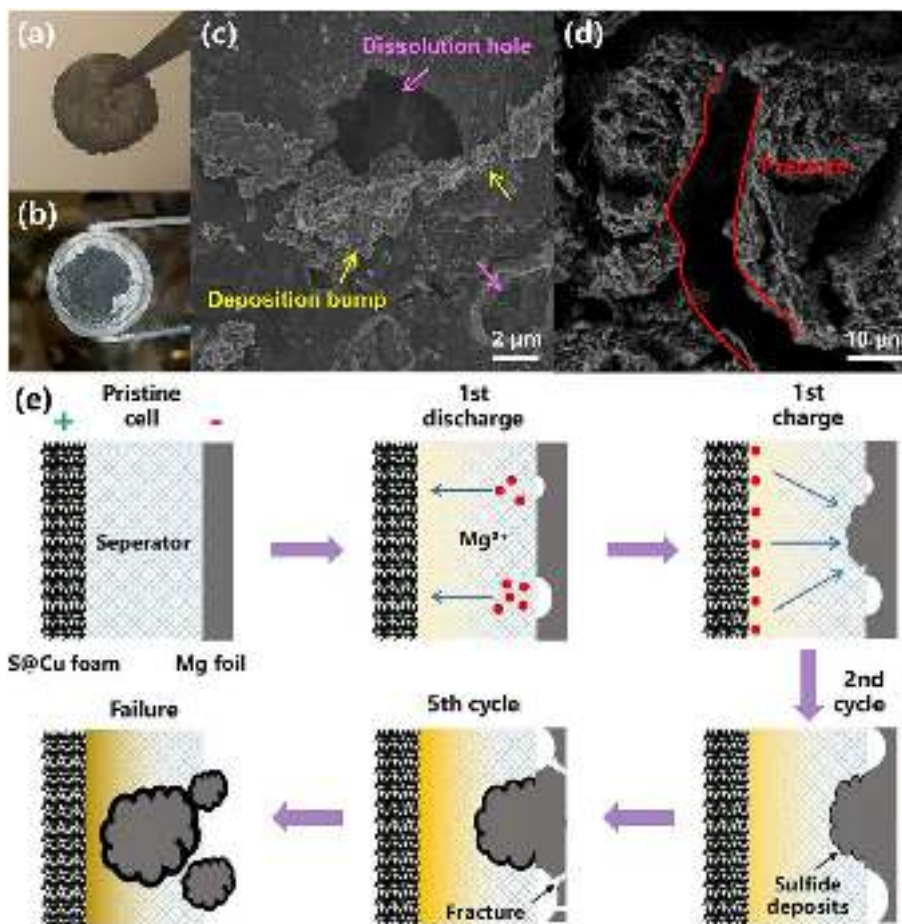


**Fig. 7.** Digital photographs of the Mg anode after 1st cycle (a) and 6th cycle (b) in high area capacity Mg-metal battery. SEM images of the Mg anode after 1st cycle (c) and 6th cycle (d). Schematic illustration of cell failure mechanism (e).

cell performance degradation. Another chief aim of this work is to ascertain the cell failure mechanism and the hidden safety hazard.

To identify the major reason leading to cell failure, the Mg stripping/plating processes with controlled area-capacity ( $30 \text{ mAh cm}^{-2}$ ) are investigated. As shown in Fig. 6(a and b), the voltage hysteresis during initial Mg stripping and plating processes is about 280 mV, which shows a relative stable value of 200 mV during subsequent cycles until a short circuit happens at 15th cycle. The Coulombic efficiency also declines from 98.6% (2nd cycle) to 94.3% (10th cycle). As clearly shown in Fig. 6(g), the higher the area capacity, the shorter the cycle life of asymmetric Cu-Mg cell will be obtained. The pristine Mg anode with metallic luster shows a relative smooth surface with aligned shallow polishing gully as shown in Fig. 6(c) and the inset photo in Fig. 6(c). The cycled Mg anode tarnishes and the dissolving pits are observed after the initial discharge process (Fig. 6d and the inset photo in Fig. 6d). The re-deposits shown in Fig. 6(e) display non-dendritic morphology while the growth of Mg embeds into and pierces through the thick glass fiber separator. After 15 stripping/plating cycles, SEM image in Fig. 6(f) reveals the pancake morphology of Mg deposit locally and the Mg anode completely darkens and becomes loose, porous, and thicker compared with its initial state (inset in Fig. 6f).

Schematically shown in Fig. 6(h), the desired Mg electrode-deposits should distribute uniformly on the surface of Mg anode without penetrating into the large pores of glass fiber separators. The realistic (see Fig. 6i), however, is that the extremely nonuniform topography is shown on the surface of deeply cycled Mg anode, in which the Mg deposits tend to fulfil the large opening space in glass fiber separators. These above analyses of cycled

Mg anodes reveal the fact that nonuniform Mg surface topography may be a major culprit for cell performance degradation and even cell failure.

The cycled S@Cu foam||Mg full cells are also monitored to check out the influences of whole cell components on their lifespan. A cellulose-glass fiber-cellulose sandwich separator is used in full cell configuration in order to exclude the fast internal short circuit by Mg-metal anode as discussed above. Compared with digital photograph of pristine Mg anode in Fig. 6(c), tarnish and asperity are observed on the surface of the Mg anode after merely the 1st cycle (Fig. 7a). SEM image (Fig. 7c) reveals the existence of both dissolution holes and large deposited protrusions, which may be ascribed to the spatial inhomogeneity in current distribution as revealed by our previous work [37,38]. More interestingly, the Mg anode completely darkens and is broken into pieces after the 6th cycle (Fig. 7b). SEM images (Fig. 7d) further demonstrate the appearance of considerable fractures which result in pulverization of the Mg anode after the 6th cycle (Fig. S16). The EDS (energy dispersive spectroscopy)-mapping image (Fig. S17) and the XPS data (Fig. S18) of cycled Mg anodes also reveal the presence of shuttle effect of both polysulfide species and copper-containing species during battery cycling, which further accelerate the corrosion of Mg anodes. On the one hand, the partial dissolution of cuprous-ions can facilitate the electrode kinetics due to the fast conversion liquid-solid processes (compared with the solid to solid processes). On the other hand, the shuttle of the cuprous-ions may deteriorate the Mg anode seriously, which results in unsatisfied cycle life for high mass loading electrodes. Digital photographs (Fig. S19) and SEM images (Fig. S20) of the sandwich separator illustrate that it has been pierced by the irregular and stiff Mg deposits.



This fact suggests that despite of non-dendritic morphology, the nonuniform Mg anode surface topography is truly one of the potential safety hazards for Mg metal-based cells especially under practical operational conditions.

Worth noting is that the S@Cu foam cathodes with ultrahigh capacity of  $\sim 30 \text{ mAh cm}^{-2}$  also undergo conversion reactions accompanied by dramatic volume changes during charge and discharge as shown in Figs. S21 and S22. This may be possibly incapable of leading to cell failure because the large pore and skeleton framework of copper foam can effectively accommodate the volume change. However, as to the Mg anode, the re-deposition of Mg may not fill in the dissolution holes (shown in Fig. 7c) owing to the much higher current density on protrusions than that on the surrounding surface. To verify this assumption, as shown in Fig. S23, the reassembled cell is able to cycle for twice at a current density of  $0.1 \text{ mA cm}^{-2}$ , which displays a high area capacity of  $8.3 \text{ mAh cm}^{-2}$ . Thus, although there is sufficient space for the re-deposition of Mg, the recharging process of Mg-metal full cells tends to cause the penetration of separator by Mg deposits, leading the ultimate cell failure as schematically depicted in Fig. 7(e). These new findings not only experimentally validate the underlying safety hazard for the first time, but also highlight the need to control homogeneous and smooth growth of metallic Mg anode for practical Mg batteries.

### 3. Conclusions

In summary, this work successfully implements Mg batteries with high area-capacity by the sulfur/copper integrated cathodes. Both the cathode reaction pathway and Mg-metal anode failure mechanism are systematically investigated. Specifically, on the cathode side, the in-situ formed copper sulfide intermediates are revealed to act as an intermediate, which is beneficial for the transformation of sulfur to rock-salt MgS during the first discharge process. First-principle calculations reveal that the existence of Cu defects in the copper sulfide lattice significantly lowers the energy barrier of the electrochemical injection of  $\text{Mg}^{2+}$  and essentially improves the diffusive ability of both  $\text{Mg}^{2+}$  and  $\text{Cu}^+$  in electrodes, which makes substantial contribution in driving the fast displacement reaction between copper sulfide active substances and MgS. On the anode side, the nonuniform Mg deposits derived from the spatial inhomogeneity of current distribution during charge-discharge processes are for the first time demonstrated to lead to the gradual battery performance degradation and even pose potential safety hazards for practical Mg batteries with an ultrahigh areal capacity of around  $30 \text{ mAh cm}^{-2}$ . Both the area-capacity-improvement strategy and Mg-metal anode failure mechanism offer new fundamental insights and understandings on the research of high performance Mg batteries.

### Declaration of competing interest

The authors declare that they have no known competing financial interests or personal.

### Acknowledgments

This work was supported by the National Natural Science Foundation of China (21805157, 51972187), the Project funded by China Postdoctoral Science Foundation (2021M701817), the Natural Science Foundation of Shandong Provincial (ZR2021QE166), the National Natural Science Foundation for Distinguished Young Scholars of China (51625204), and the Major Basic Research Program of Natural Science Foundation of Shandong Province (ZR2020ZD09).

### Appendix A. Supplementary data

Supplementary data to this article can be found online at <https://doi.org/10.1016/j.jechem.2022.05.046>.

### References

- [1] R. Mohtadi, O. Tutusaus, T.S. Arthur, Z. Zhao-Karger, M. Fichtner, *Joule* 5 (2021) 581–617.
- [2] Y. Tian, G. Zeng, A. Rutt, T. Shi, H. Kim, J. Wang, J. Koettgen, Y. Sun, B. Ouyang, T. Chen, Z. Lun, Z. Rong, K. Persson, G. Ceder, *Chem. Rev.* 121 (2021) 1623–1669.
- [3] Y.L. Liang, H. Dong, D. Aurbach, Y. Yao, *Nat. Energy* 5 (2020) 646–656.
- [4] D.T. Nguyen, R. Horia, A.Y.S. Eng, S.W. Song, Z.W. Seh, *Mater. Horizons* 8 (2021) 830–853.
- [5] C.L. You, X.W. Wu, X.H. Yuan, Y.H. Chen, L.L. Liu, Y.S. Zhu, L.J. Fu, Y.P. Wu, Y.G. Guo, T. van Ree, *J. Mater. Chem. A* 8 (2020) 25601–25625.
- [6] Y. Xu, Y.X. Zhao, S.Y. Zhao, J.F. Zhang, J. Li, J.H. Guo, Y.G. Zhang, *Energy Storage Mater.* 42 (2021) 513–516.
- [7] L. Kong, C. Yan, J.Q. Huang, M.Q. Zhao, M.M. Titirici, R. Xiang, Q. Zhang, *Energy Environ. Mater.* 1 (2018) 100–112.
- [8] T. Gao, X. Ji, S. Hou, X.L. Fan, X.G. Li, C.Y. Yang, F.D. Han, F. Wang, J.J. Jiang, K. Xu, C.S. Wang, *Adv. Mater.* 30 (2018) 1704313.
- [9] B.P. Vinayan, H. Euchner, Z. Zhao-Karger, M.A. Cambaz, Z.Y. Li, T. Diemant, R.J. Behm, A. Gross, M. Fichtner, *J. Mater. Chem. A* 7 (2019) 25490–25502.
- [10] X.D. Hong, J. Mei, L. Wen, Y.Y. Tong, A.J. Vasilieff, L.Q. Wang, J. Liang, Z.Q. Sun, S. X. Dou, *Adv. Mater.* 31 (2019) 1802822.
- [11] P. Canepa, G.S. Gautam, D.C. Hannah, R. Malik, M. Liu, K.G. Gallagher, K.A. Persson, G. Ceder, *Chem. Rev.* 117 (2017) 4287–4341.
- [12] D. Wu, W. Ren, Y.N. NuLi, J. Yang, J.L. Wang, *J. Mater. Sci. Technol.* 91 (2021) 168–177.
- [13] H. Dong, O. Tutusaus, Y.L. Liang, Y. Zhang, Z. Lebens-Higgins, W.L. Yang, R. Mohtadi, Y. Yao, *Nat. Energy* 5 (2020) 1043–1050.
- [14] G.L. Zhu, G.L. Xia, X.B. Yu, *Small* 17 (2021) 2101845.
- [15] Y.L. Shen, Y.J. Wang, Y.C. Miao, M. Yang, X.Y. Zhao, X.D. Shen, *Adv. Mater.* 32 (2020) 1905524.
- [16] S.Y. Hou, X. Ji, K. Gaskell, P.F. Wang, L.N. Wang, J.J. Xu, R.M. Sun, O. Borodin, C.S. Wang, *Science* 374 (2021) 172–178.
- [17] J.T. Herb, C.A. Nist-Lund, C.B. Arnold, *ACS Energy Lett.* 1 (2016) 1227–1232.
- [18] W. Ren, D. Wu, Y.N. NuLi, D. Zhang, Y. Yang, Y. Wang, J. Yang, J.L. Wang, *ACS Energy Lett.* 6 (2021) 3212–3220.
- [19] J.H. Ha, B. Lee, J.H. Kim, B.W. Cho, S.-O. Kim, S.H. Oh, *Energy Storage Mater.* 27 (2020) 459–465.
- [20] M. Mao, T. Gao, S. Hou, F. Wang, J. Chen, Z. Wei, X. Fan, X. Ji, J. Ma, C. Wang, *Nano Lett.* 19 (2019) 6665–6672.
- [21] C. Wu, J. Hu, J. Tian, F. Chu, Z. Yao, Y. Zheng, D. Yin, C. Li, *ACS Appl. Mater. Interfaces* 11 (2019) 5966–5977.
- [22] A. Robba, M. Mežnar, A. Vizintin, J. Bitenc, J. Bobnar, I. Arčon, A. Randon-Vitanova, R. Dominko, *J. Power Sources* 450 (2020) 227672.
- [23] D. Huang, S. Tan, M. Li, D. Wang, C. Han, Q. An, L. Mai, *ACS Appl. Mater. Interfaces* 12 (2020) 17474–17480.
- [24] Z.H. Zhang, B.B. Chen, H.M. Xu, Z.L. Cui, S.M. Dong, A.B. Du, J. Ma, Q.F. Wang, X. H. Zhou, G.L. Cui, *Adv. Funct. Mater.* 28 (2018) 1701718.
- [25] L. Zeng, N. Wang, J. Yang, J. Wang, Y. NuLi, *J. Electrochem. Soc.* 164 (2017) A2504–A2512.
- [26] Z. Zhang, Z. Cui, L. Qiao, J. Guan, H. Xu, X. Wang, P. Hu, H. Du, S. Li, X. Zhou, S. Dong, Z. Liu, G. Cui, L. Chen, *Adv. Energy Mater.* 7 (2017) 1602055.
- [27] X.Y. Cheng, Z.H. Zhang, Q.Y. Kong, Q.H. Zhang, T. Wang, S.M. Dong, L. Gu, X. Wang, J. Ma, P.X. Han, H.J. Lin, C.T. Chen, G.L. Cui, *Angew. Chem. Int. Ed.* 59 (2020) 11477–11482.
- [28] Y.L. Shen, Q.H. Zhang, Y.J. Wang, L. Gu, X.Y. Zhao, X.D. Shen, *Adv. Mater.* 33 (2021) 2103881.
- [29] H.D. Yoo, Y. Liang, H. Dong, J. Lin, H. Wang, Y. Liu, L. Ma, T. Wu, Y. Li, Q. Ru, Y. Jing, Q. An, W. Zhou, J. Guo, J. Lu, S.T. Pantelides, X. Qian, Y. Yao, *Nat. Commun.* 8 (2017) 339.
- [30] T. Koketsu, J. Ma, B.J. Morgan, M. Body, C. Legein, W. Dachraoui, M. Giannini, A. Demortière, M. Salanne, F. Dardozze, H. Groult, O.J. Borkiewicz, K.W. Chapman, P. Strasser, D. Dambournet, *Nat. Mater.* 16 (2017) 1142.
- [31] A. Robba, A. Vizintin, J. Bitenc, G. Mali, I. Arčon, M. Kavčič, M. Žitnik, K. Bučar, G. Aquilanti, C. Martineau-Corcós, A. Randon-Vitanova, R. Dominko, *Chem. Mater.* 29 (2017) 9555–9564.
- [32] H.S. Kim, T.S. Arthur, G.D. Allred, J. Zajicek, J.G. Newman, A.E. Rodnyansky, A.G. Oliver, W.C. Boggess, J. Muldoon, *Nat. Commun.* 2 (2011) 427.
- [33] Z. Zhao-Karger, X. Zhao, D. Wang, T. Diemant, R.J. Behm, M. Fichtner, *Adv. Energy Mater.* 5 (2015) 1401155.
- [34] F. Xiong, Y. Fan, S. Tan, L. Zhou, Y. Xu, C. Pei, Q. An, L. Mai, *Nano Energy* 47 (2018) 210–216.
- [35] C. Coughlan, M. Ibáñez, O. Dobrozhan, A. Singh, A. Cabot, K.M. Ryan, *Chem. Rev.* 117 (2017) 5865–6109.
- [36] H. Liu, X. Shi, F. Xu, L. Zhang, W. Zhang, L. Chen, Q. Li, C. Uher, T. Day, G.J. Snyder, *Nat. Mater.* 11 (2012) 422.
- [37] Z.H. Song, Z.H. Zhang, A.B. Du, S.M. Dong, G.C. Li, G.L. Cui, *J. Energy Chem.* 48 (2020) 299–307.
- [38] Z.H. Song, Z.H. Zhang, A.B. Du, S.M. Dong, G.C. Li, G.L. Cui, *Adv. Mater.* 33 (2021) 2100224.